Article

Global apparent temperature sensitivity of terrestrial carbon turnover modulated by hydrometeorological factors

Naixin Fan [1,2] ✉, **Markus Reichstein** [1,3], **Sujan Koirala** [1], **Bernhard Ahrens** [1], **Miguel D. Mahecha** [4,5] & **Nuno Carvalhais** [1,3,6] ✉

The ecosystem carbon turnover time—an emergent ecosystem property that partly determines the feedback between the terrestrial carbon cycle and climate—is strongly controlled by temperature. However, it remains uncertain to what extent hydrometeorological conditions may influence the apparent temperature sensitivity of τ, defined as the factor by which the carbon turnover time increases with a 10 °C rise in temperature (Q_{10}). Here, we investigate the responses of the ecosystem carbon turnover to temperature and hydrometeorological factors using an ensemble of observation-based global datasets and a global compilation of in situ measurements. We find that temperature and hydrometeorology are almost equally important in shaping the spatial pattern of ecosystem carbon turnover, explaining 60 and 40% of the global variability, respectively. Accounting for hydrometeorological effects puts a strong constraint on Q_{10} values with a substantial reduction in magnitude and uncertainties, leading Q_{10} to converge to 1.6 ± 0.1 globally. These findings suggest that hydrometeorological conditions modulate the apparent temperature sensitivity of terrestrial carbon turnover times, confounding the role of temperature in quantifying the response of the carbon cycle to climate change.

The net exchange of CO_2 between the atmosphere and the terrestrial biosphere is determined by carbon uptake via photosynthesis and carbon turnover time (τ)[1–4]. The response of τ to climate change is poorly constrained by observations, as reflected by substantial uncertainties in current simulations of climate–carbon cycle feedback[4–6]. One central challenge in understanding the feedback between the terrestrial carbon cycle and climate is quantifying the temperature sensitivity of carbon turnover time in terrestrial ecosystems. Although there is a general consensus that temperature is a crucial driver of τ (refs. [2,3,7,8]), the sensitivity of τ to temperature and its dependence on different

climate conditions is subject to much debate[3,8–10]. Previous studies showed evidence that the long-term (multi-decadal) apparent temperature sensitivity of terrestrial carbon turnover increases with temperature[3]. However, this dependency was not found at the ecosystem level and at a decadal temporal scale in other studies[11,12]. Moreover, it still remains unclear how changes in hydrometeorological conditions may affect the apparent temperature sensitivity of τ since a notable spatial correlation between precipitation and τ has been found[2]. Globally, hydrometeorological conditions largely determine soil water availability and therefore influence the carbon turnover process by

[1]Max Planck Institute for Biogeochemistry, Jena, Germany. [2]Institute of Photogrammetry and Remote Sensing, Technische Universität Dresden, Dresden, Germany. [3]ELLIS Unit Jena, Jena, Germany. [4]Remote Sensing Centre for Earth System Research, Leipzig, Germany. [5]Helmholtz Centre for Environmental Research, Leipzig, Germany. [6]Departamento de Ciências e Engenharia do Ambiente, Faculdade de Ciências e Tecnologia, Universidade Nova de Lisboa, Caparica, Portugal. ✉e-mail: nfan@bgc-jena.mpg.de; ncarvalhais@bgc-jena.mpg.de

controlling soil respiration and decomposition processes[8,13,14]. Currently, a comprehensive understanding of the climatic controls on the long-term temperature sensitivity of τ is still lacking. Here, we contrast the spatial responses of τ to large-scale climatic gradients to quantify the dominant factors behind the spatial variability in carbon turnover times at different spatial scales. We assess the apparent spatial temperature sensitivity of τ, quantified as the change in turnover time with a 10 °C rise in temperature under the influence of other environmental factors (Q_{10}). The concept of apparent temperature sensitivity is used here as contrast to intrinsic temperature sensitivity since, in reality, the response of turnover time to temperature is simultaneously affected by other environmental changes[3,8]. Our aim is to quantify the variability of Q_{10} across different terrestrial ecosystems to address the question: 'To what extent can hydrometeorological conditions influence the temperature sensitivity of τ?'.

Direct determination of the transient response of τ to climate is hampered by a lack of long-term dynamical observations of carbon storage (including soil and vegetation). An alternative is to infer emergent τ–climate relationships across spatial gradients, since the spatial variability of τ reflects long-term accumulated effects of climate, productivity, respiration and ecosystem carbon storage[2,3]. Therefore, we note that Q_{10} in this study represents the climatological temperature sensitivity of τ that can be used to diagnose long-term climatic effects on carbon turnover times. Using the state-of-the-art observation-based ensemble of soil carbon stock (C_{soil}), vegetation biomass (C_{veg}), terrestrial ecosystem respiration (TER) and gross primary production (GPP), we estimated τ and its uncertainties in a full factorial way to account for the uncertainties originating from different data sources (Extended Data Figs. 1 and 2 and Supplementary Information). In a complementary approach, we also used a global compilation (over 200 sites) of τ estimates at the site level to estimate Q_{10} values and quantify the potential hydrometeorological effect at the global scale (see Methods).

We analysed each ensemble member of τ estimation independently, but in a consistent way at the global, biome and latitudinal level. To account for the effect of hydrometeorology on the temperature sensitivity of τ (hereafter, the H effect), we used mean annual precipitation (MAP), potential evapotranspiration (PET) and peat soil fraction (PSF) to represent different hydrometeorological/hydrological processes (hereafter, H factors; see Methods).

Global patterns between τ and climate

Our analysis reveals a contrasting global pattern of τ spatial variability correlated with temperature and hydrometeorological variables (Fig. 1). We show a strong linear relationship between the global distribution of logarithmic τ (log[τ], base of 10) and temperature (Fig. 1a,d), corroborating an emergent τ–temperature sensitivity at the global scale. In contrast, we find that log[τ] is inversely related to precipitation (log[τ] - 1/MAP) and PET (log[τ] - 1/PET), as confirmed by the patterns derived from both ensemble and site-level τ estimates (Fig. 1b,c,e,f). Further analysis shows that there are strong partial correlations between τ and H factors when temperature is controlled (see Supplementary Information Section 2.1), reflecting the potential controls of water availability on τ at the global scale.

To obtain the contributions of temperature and hydrometeorological conditions to the spatial variability of τ and the Q_{10} values, we decomposed the variability in logarithmic τ of each ensemble member at each spatial scale into components that are driven by mean annual temperature (MAT) and each of the H factors:

$$\log_{10}[\tau] = a_{MAT} \times MAT + \varepsilon \tag{1}$$

$$\log_{10}[\tau] = a_{MAT} \times MAT + a_{MAP} \times \frac{1}{MAP} + a_{PET} \times \frac{1}{PET} + a_{PSF} \times PSF + \varepsilon \tag{2}$$

Here, a represents the estimated sensitivity of each respective climate component and ε is the residual error term. The Q_{10} values are derived from a_{MAT} by applying the definition of Q_{10} (see Methods). We use equation (1) to derive the temperature sensitivity of τ without considering the H effect, in contrast with equation (2) in which the H effect is accounted for. To satisfy the most important mathematical assumption in linear regression—that its deterministic component is a linear function of the separate predictors[15]—we transformed MAP and PET into their inverse forms based on the emergent nonlinear patterns between τ and MAP and τ and PET (Fig. 1b,c,e,f). Thus, equations (1) and (2) are used to assess the H effect on temperature sensitivity, as well as the contributions of temperature and H factors to the changes in τ at different spatial scales.

The H effect on the apparent Q_{10} values

Examination of global observational ensemble and site-level τ estimations shows that the sensitivity of τ to temperature is substantially constrained by accounting for the H effect. Both the magnitude and the uncertainty of Q_{10} values are substantially reduced while model performances increase significantly (Extended Data Table 1) by considering the H effect globally, resulting in a median Q_{10} value of 1.6 with an interquartile range (IQR) from 1.5 to 1.7 (1.6 ± 0.1), compared with 2.2 ± 0.2 when the H effect is not considered (Fig. 2). Similar results are found with independent site-level data, where Q_{10} values are reduced from 1.9 ± 0.1 to 1.6 ± 0.1 by accounting for the H effect (Fig. 2). Consequently, the global temperature sensitivity of τ is confounded by H factors. Our results indicate that both temperature and hydrometeorological conditions are critical in explaining the spatial variability of τ at the global scale. We further investigated potential influences of topography, climate seasonality and land use change on the residuals of modelled τ. Our results show that these factors play a marginal role in explaining the residual patterns of modelled τ at a large spatial scale (see Supplementary Information Section 2.2).

In contrast with a previous study[3], our results show a much-reduced range of Q_{10} values across global temperature gradients by accounting for the H effect, challenging the temperature dependency in spatial Q_{10} patterns (see Supplementary Information Section 3 for details). By considering the H effect for the global fitting (via equation (2)), we find 66–88% reductions in the range of Q_{10} values and a change in the relationship between log[τ] and temperature from a quadratic to a linear function, challenging the Q_{10} dependence on temperature. This is supported by further statistical analysis using different ensemble datasets and site-level observations (Extended Data Figs. 3 and 4 and Supplementary Information).

Relative importance of temperature and H factors

To quantify the relative importance of temperature and H factors, we investigated the relative dominance (RD; see Methods) of each climatic factor. Globally, we find that temperature and H factors explain approximately 60% (RD = -0.6) and 40% (RD = -0.4) of the spatial variability of τ, respectively. This pattern is consistent across different ensemble members, showing an RD of temperature of 0.6 ± 0.1 and of H factors of 0.4 ± 0.1, respectively. Similar results are also found at the site level (Table 1). Although spatial turnover times have long been thought to be dominated by the large spatial gradient of temperature[1–3,7], our study shows that H factors are almost equally as important as temperature in explaining spatial τ variability. These results further suggest that abstracting from the effects that H factors have on the variability of τ may cause biases in determining a spatial τ–temperature sensitivity.

Roles of climate factors and estimated Q_{10} values

The RDs of temperature (RD_T) and H factors (RD_H) are heterogeneous across different biomes (see Supplementary Fig. 4.1 for the spatial distribution of biomes). Temperature plays a dominant role in temperate grassland (RD_T = 72%) and semi-arid grassland (RD_T = 57%),
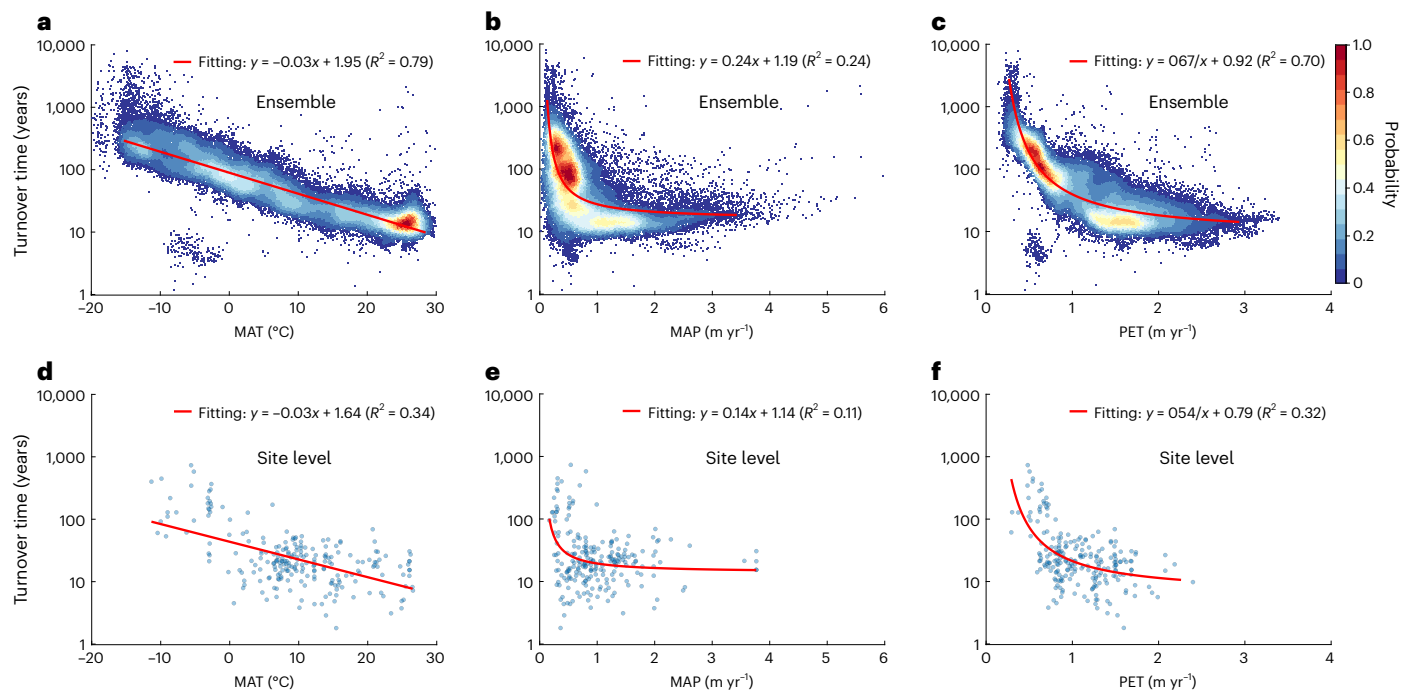
Fig. 1 | Global τ–climate patterns derived from ensemble median and in situ τ datasets. a–c, Density distribution plots for logarithmic τ (base of 10) versus MAT (**a**), MAP (**b**) and PET (**c**) using the gridded mean ensemble dataset. **d–f**, Scatter plots of logarithmic τ (base of 10) versus MAT (**d**), MAP (**e**) and PET (**f**) using the in situ dataset. The red lines in **a** and **d** represent the fitting between logarithmic τ and MAT as a linear function ($\log_{10}[\tau] \sim ax + b$) and the red lines in **b**, **c**, **e** and **f** represent the fitting between logarithmic τ and MAP or PET as an inverse function ($\log_{10}[\tau] \sim a(1/x) + b$). The parameters of each fitting and the R^2 values between each climatic component and τ are provided in the legend.
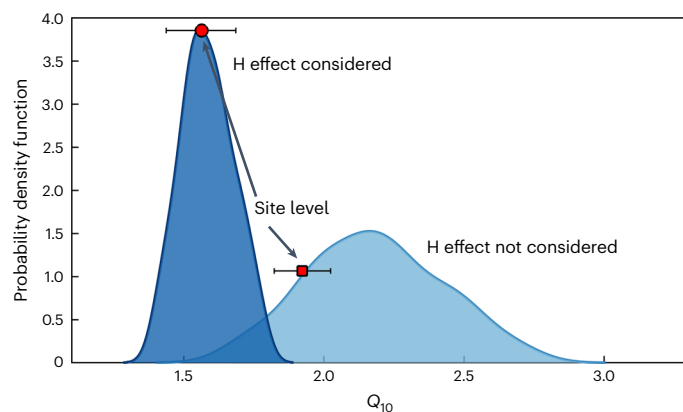
Fig. 2 | H effect on Q_{10} values at the global scale. Comparison between the probability density of Q_{10} values (derived from all ensemble members of τ estimates; sample size, $n = 144$) estimated using only temperature (equation (1)) and considering both temperature and H factors (equation (2)) reveals substantially constrained Q_{10} values after the H effect is considered. Independent estimations of Q_{10} values using site-level data are indicated by the red square (H effect not considered) and red circle (H effect considered). The error bars indicate the median bounded by the IQR (median ± IQR/2) of Q_{10} estimations from bootstrapping (sample size, $n = 1,000$) site-level data.

whereas it contributes less to the τ variability in tropical forest ($RD_T = 47\%$), temperate forest ($RD_T = 48\%$), wetland ($RD_T = 48\%$) and cropland ($RD_T = 35\%$) ecosystems (Fig. 3a). H factors are dominant in boreal forests ($RD_H = 92\%$), tundra ($RD_H = 89\%$) and tropical savannahs ($RD_H = 70\%$) where most of the contribution to the τ variability emerges from precipitation and PET patterns, rather than from temperature (Fig. 3a). However, the results in tropical forests and tropical

savannahs are probably challenged by poor model performances in these regions (Supplementary Fig. 4.2), which are associated with a low spatial variability in τ and reduced spatial temperature gradients (Supplementary Fig. 4.3). The contribution of H factors to the variability of τ is also reflected when determining Q_{10} at the biome level. Figure 3b shows that Q_{10} values are adjusted to higher values in tropical forest, whereas they are suppressed in the other ecosystems, especially in tundra and boreal forests, by accounting for the H effect. The importance of the peatland fraction emerges in boreal, tropical and wetland ecosystems, as shown by the higher RD of PSF (Fig. 3). The significant positive τ–PSF correlations in those biomes (Supplementary Fig. 4.6) indicate that the interaction between soil/vegetation dynamics and the hydrological cycle can substantially influence carbon turnover times at the local scale[16,17]. Overall, both across-biome variability and within-biome uncertainty in Q_{10} estimates are substantially decreased by accounting for H factors: Q_{10} across biomes reduces from 1.9 ± 0.3 to 1.4 ± 0.2, while the within-biome uncertainty in τ decreases overall by 10% (Fig. 3b). The uncertainties of Q_{10} estimates are substantially reduced in temperate forest (by 27%), boreal forest (by 34%) and tundra (by 15%).

In tundra and boreal forests, we observe a linear (negative) response of τ to PET, while the temperature sensitivities are strongly reduced when accounting for H factors, indicating a dominant role of PET in these biomes (Fig. 3a,b). We investigated the potential link between τ and PET by analysing the relationship between PET and each of the different ecosystem components (see details in Supplementary Information Section 4). We find strong positive correlations between carbon fluxes (GPP and TER), vegetation biomass and PET while controlling for other climatic factors, whereas no such pattern is found between PET and soil carbon stock (Supplementary Figs. 4.7 and 4.8). This finding indicates that vegetation biomass and GPP (and TER) increase with higher PET in tundra and boreal biomes, but that the soil carbon stock does not follow that trend. We further show a

Table 1 | Comparison of Q_{10} values and the RD of each climate variable based on ensemble median and site-level data

Data type	Q_{10} (H effect not considered)	Q_{10} (H effect considered)	RD_{MAT} (%)	RD_{MAP} (%)	RD_{PET} (%)	RD_{Peat} (%)
Site level	1.92±0.12	1.56±0.12	61.05±14.28	3.90±3.43	26.19±12.22	8.78±6.34
Ensemble	2.17±0.16	1.56±0.06	60.75±11.58	6.80±5.01	31.38±15.05	1.07±1.63

The uncertainty bounds represent the spread (IQR) among all ensemble members (n=144).
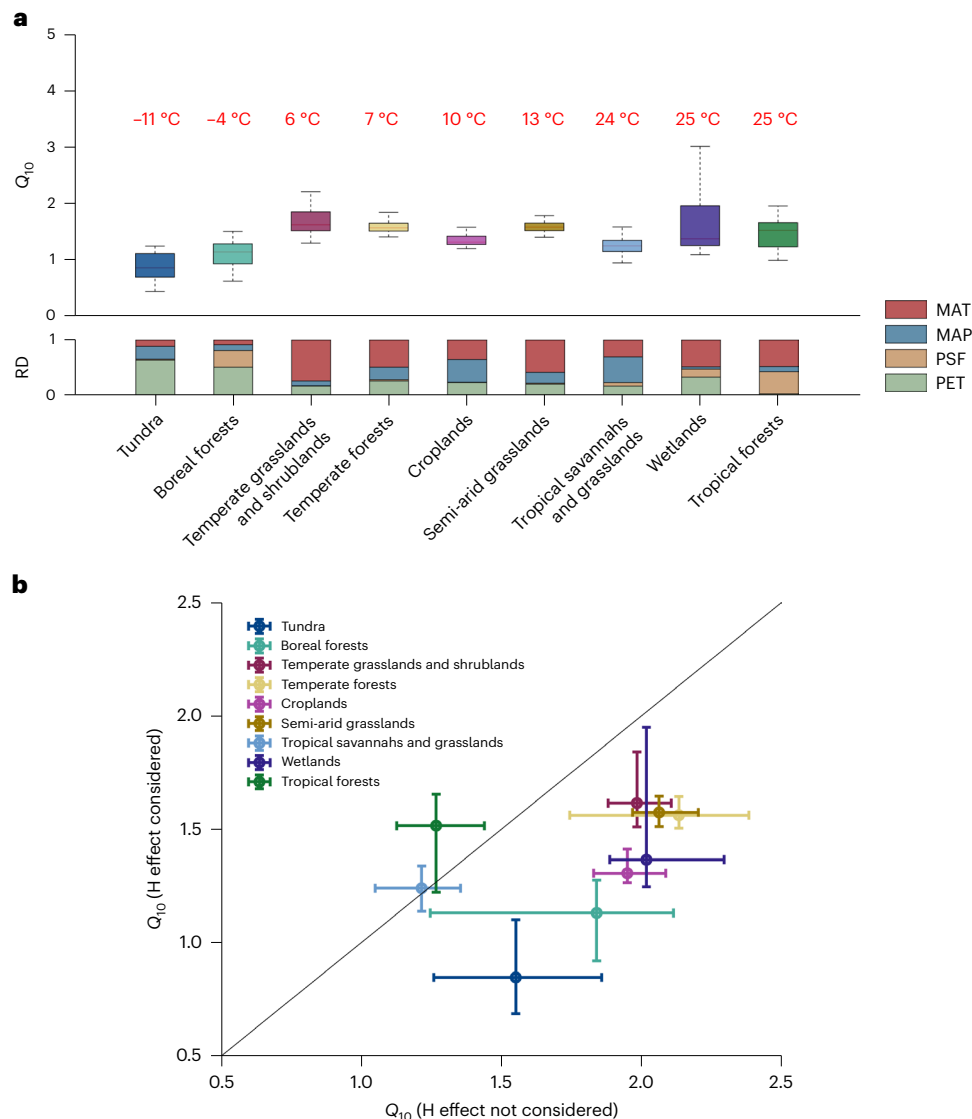
Fig. 3 | Estimation of Q_{10} values at the biome level and the RD of temperature and H factors. a, Estimation of median Q_{10} values with the H effect considered. The RDs of climate variables are shown by a stacked bar plot. The biomes are ordered (ascending) by the average MAT of each biome, which is shown above each box plot. The sample size of each biome is n = 144 (all ensemble members). For each box plot, the central red mark represents the median and the bottom and top edges indicate the 25th and 75th percentiles, respectively. The boxes extend to the minimum and maximum values that are not considered outliers. **b**, Comparison of the Q_{10} values with and without the H effect considered. The error bars show the uncertainty (IQR) derived from different ensemble members (n = 144). The vertical and horizontal error bars correspond to the uncertainties of the Q_{10} values with and without the H effect considered, respectively. The 1:1 reference line (black) is plotted to compare the relative values of two estimations.

linear decrease of τ with higher vegetation biomass (Supplementary Fig. 4.9), indicating that a faster carbon turnover in response to higher PET can possibly be caused by: (1) a priming effect, which would stimulate decomposition processes when there are inputs of fresh carbon into deeper soil layers[18]; and (2) an increase in available energy for the decomposition of carbon[8]. However, given the co-variation between PET and MAT, especially at high latitudes (Supplementary Fig. 5.4), which makes it difficult to fully decouple these factors, the hypotheses stand as outstanding questions that need addressing to further grasp the effects of future changes in climate on τ.
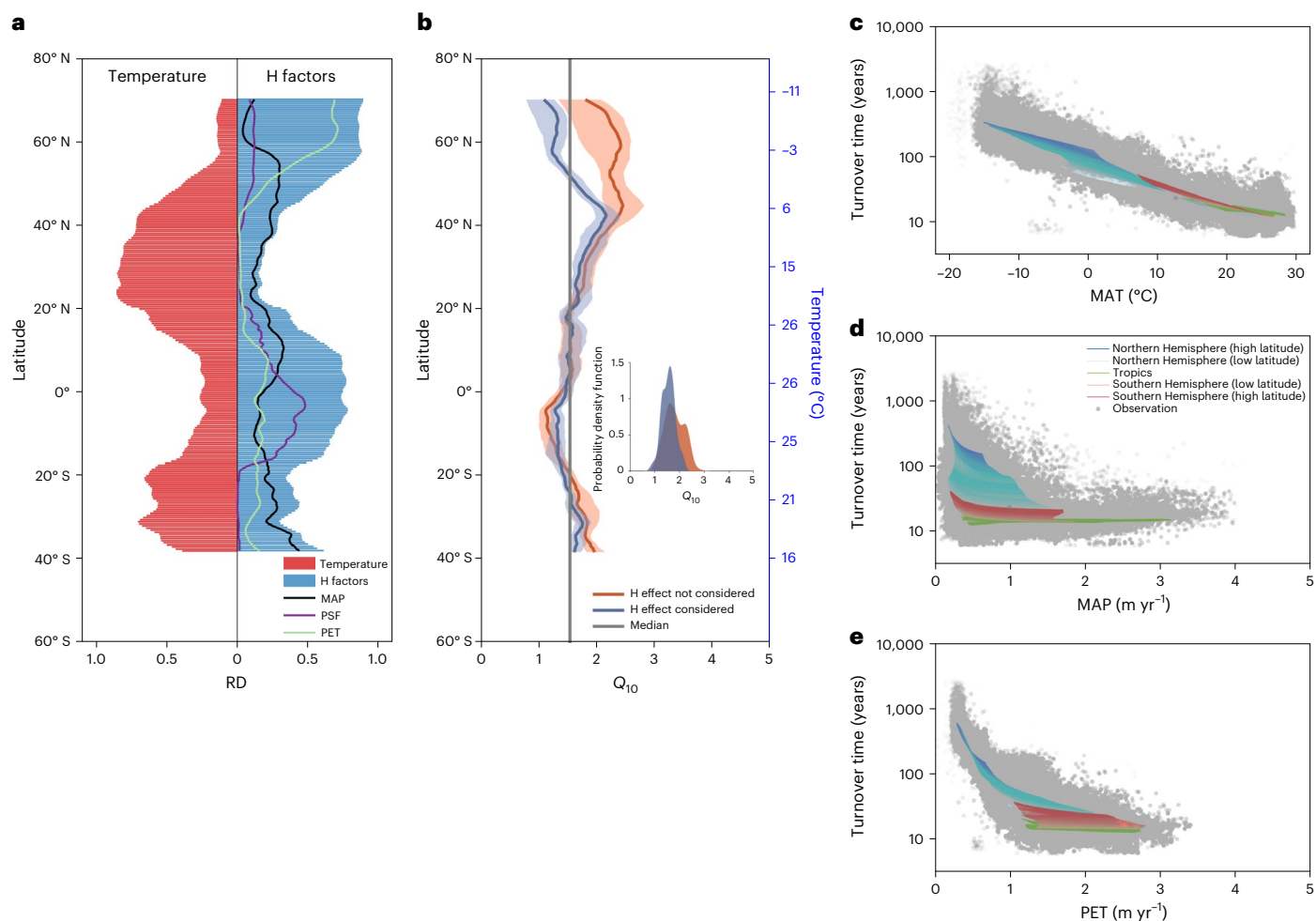
Fig. 4 | Latitudinal patterns of RD and temperature sensitivity of τ to MAT along latitude. a, RDs of temperature and H factors across latitude. **b**, Comparison of median Q_{10} values with (purple) and without (orange) hydrometeorological control. The uncertainty bounds shown as shaded areas represent the spread (IQR) among all ensemble members ($n = 144$). The inset figure shows the comparison of probability density estimates of Q_{10} values. The grey vertical line indicates the median value of Q_{10} with hydrometeorological control. The latitudes >70° N and <40° S are excluded due to little land area

coverage. **c**, Regression between $\log[\tau]$ and MAT for each moving window across latitudes. Each line represents one fitting between τ and MAT in a latitudinal window (see Methods). The blue, red and green lines represent the Northern Hemisphere (20° N–60° N), Southern Hemisphere (20° S–60° S) and tropics (20° N–20° S), respectively. Overlay points in grey are observations. Deeper colours represent higher latitudes and vice versa. **d,e**, Responses of $\log[\tau]$ to MAP (**d**) and PET (**e**). Each curve represents the fitted inverse function between τ and MAP/PET in a latitudinal window.

Our analysis shows large variability in the RD of temperature and H factors across latitude (see Methods and Supplementary Information Section 5 for details). Consistent with our previous results at the biome level, we show that temperature plays a more important role at temperate and subtropical latitudes, whereas H factors dominate the τ variability at high northern latitudes (>55° N) (Fig. 4a). Compared with the pattern at the global scale, the increasing spatial variability in the RD at the latitudinal scale indicates a much higher heterogeneity when local features are considered. Despite the heterogeneity in the RD of temperature and H factors, our analysis reveals highly consistent linear τ–temperature patterns across latitude (Fig. 4c, slope = −0.024 ± 0.007) as well as an apparent inverse relationship between τ and MAP and τ and PET (Fig. 4d,e). The sensitivity of τ to PET increases with higher latitude, which is in line with the result of a higher importance of PET at high latitudes. Factoring in the contributions of H factors in determining the temperature sensitivity of τ results in constrained Q_{10} values (1.5 ± 0.2), in contrast with the Q_{10} values (1.8 ± 0.3) obtained without considering the H effect at the latitudinal level. The H effect on temperature sensitivity is evident, especially at high northern latitudes where Q_{10} values are more constrained than at lower latitudes (Fig. 4b).

Implications for understanding carbon cycle–climate feedback

Our results highlight a fundamental yet neglected influence of hydrometeorology on the response of carbon turnover times to temperature. Supported by a large ensemble of observation-based as well as site-level τ estimates, the findings of our study suggest that hydrometeorological conditions are almost as important as temperature in shaping the spatial variability of carbon turnover times from global to latitudinal spatial scales. Despite large spatial variability in the RD of the effects of different climate factors on τ, ignoring H factors may render large biases and uncertainties when estimating the apparent sensitivity of carbon turnover times to temperature. An inclusive approach (that is, integrating H factors) yields a strong constraint on Q_{10} values with a substantial decrease in their magnitude and variability, revealing a convergence in the response of spatial turnover times to temperature when the H effect is considered. Our findings suggest that hydrometeorological conditions modulate the apparent temperature sensitivity of terrestrial carbon turnover times, confounding the role of temperature in quantifying climate–carbon cycle feedbacks. Ultimately, these results emphasize the importance of considering the spatial covariance

among climate variables in determining the strength of climate–carbon cycle feedback.

Online content

Any methods, additional references, Nature Portfolio reporting summaries, source data, extended data, supplementary information, acknowledgements, peer review information; details of author contributions and competing interests; and statements of data and code availability are available at https://doi.org/10.1038/s41561-022-01074-2.

References

1. Bloom, A. A., Exbrayat, J.-F., van der Velde, I. R., Feng, L. & Williams, M. The decadal state of the terrestrial carbon cycle: global retrievals of terrestrial carbon allocation, pools, and residence times. *Proc. Natl Acad. Sci. USA* **113**, 1285–1290 (2016).
2. Carvalhais, N. et al. Global covariation of carbon turnover times with climate in terrestrial ecosystems. *Nature* **514**, 213–217 (2014).
3. Koven, C. D., Hugelius, G., Lawrence, D. M. & Wieder, W. R. Higher climatological temperature sensitivity of soil carbon in cold than warm climates. *Nat. Clim. Change* **7**, 817–822 (2017).
4. Friend, A. D. et al. Carbon residence time dominates uncertainty in terrestrial vegetation responses to future climate and atmospheric CO_2. *Proc. Natl Acad. Sci. USA* **111**, 3280–3285 (2014).
5. Friedlingstein, P. et al. Climate–carbon cycle feedback analysis: results from the C4MIP model intercomparison. *J. Clim.* **19**, 3337–3353 (2006).
6. Todd-Brown, K. et al. Causes of variation in soil carbon simulations from CMIP5 Earth system models and comparison with observations. *Biogeosciences* **10**, 1717–1736 (2013).
7. Bird, M. I., Chivas, A. R. & Head, J. A latitudinal gradient in carbon turnover times in forest soils. *Nature* **381**, 143–146 (1996).
8. Davidson, E. A. & Janssens, I. A. Temperature sensitivity of soil carbon decomposition and feedbacks to climate change. *Nature* **440**, 165–173 (2006).
9. Fang, C., Smith, P., Moncrieff, J. B. & Smith, J. U. Similar response of labile and resistant soil organic matter pools to changes in temperature. *Nature* **433**, 57–59 (2005).
10. Reichstein, M. et al. Temperature sensitivity of decomposition in relation to soil organic matter pools: critique and outlook. *Biogeosciences* **2**, 317–321 (2005).
11. Giardina, C. P. & Ryan, M. G. Evidence that decomposition rates of organic carbon in mineral soil do not vary with temperature. *Nature* **404**, 858–861 (2000).
12. Hakkenberg, R. et al. Temperature sensitivity of the turnover times of soil organic matter in forests. *Ecol. Appl.* **18**, 119–131 (2008).
13. Hursh, A. et al. The sensitivity of soil respiration to soil temperature, moisture, and carbon supply at the global scale. *Glob. Change Biol.* **23**, 2090–2103 (2017).
14. Reichstein, M. & Beer, C. Soil respiration across scales: the importance of a model–data integration framework for data interpretation. *J. Plant Nutr. Soil Sci.* **171**, 344–354 (2008).
15. Gelman, A. & Hill, J. *Data Analysis Using Regression and Multilevel/ Hierarchical Models* (Cambridge Univ. Press, 2006).
16. Moyano, F. E., Manzoni, S. & Chenu, C. Responses of soil heterotrophic respiration to moisture availability: an exploration of processes and models. *Soil Biol. Biochem.* **59**, 72–85 (2013).
17. Sierra, C. A., Malghani, S. & Loescher, H. W. Interactions among temperature, moisture, and oxygen concentrations in controlling decomposition rates in a boreal forest soil. *Biogeosciences* **14**, 703–710 (2017).
18. Fontaine, S. et al. Stability of organic carbon in deep soil layers controlled by fresh carbon supply. *Nature* **450**, 277–280 (2007).

Methods

The ensemble of τ estimation

We used three soil carbon datasets that were derived from upscaling a compilation of worldwide soil profiles using machine learning approaches. Note that the soil carbon dataset represents the long-term mean status (approximately for the past 50 years) of carbon stocks. We also extrapolated the gridded soil data into full soil depth to investigate the effect of depth on the climatic sensitivity of τ (ref. [19]). Four global maps of vegetation biomass stocks (above and below ground), which were based on remote-sensing data and in situ inventories, were used to account for the carbon in vegetation. We used four sets of mean annual TER and GPP datasets based on different setups (remote sensing versus remote sensing and climate forcing). The datasets were derived using two partitioning methods and multiple machine learning algorithms that were trained on the FLUXNET station observations to represent fluxes of terrestrial carbon between the biosphere and atmosphere[20]. The combination of all of the above ensemble members yielded 48 global τ maps at each soil depth (1 m, 2 m and full soil depth; that is, 144 global τ maps in total).

The SoilGrids dataset[21] provides consistent spatial predictions of soil carbon stock at depths of 5, 15, 30, 60, 100 and 200 cm at a spatial resolution of 250 m. Covariates, including 158 remote-sensing-based maps, land cover, long-term climate variables and so on, were used in training. Sanderman et al.[22] used a method similar to SoilGrids but with additional covariates. In addition to geological and climate covariates, the dataset also included land use and forest fraction change. The dataset provides carbon stock at soil depths of 0–30, 30–100 and 100–200 cm at a spatial resolution of 10 km. We also used a soil carbon dataset provided by the LandGIS group[23]. The dataset provides carbon stock at depths of 10, 30, 60, 100 and 200 cm. Due the heterogeneity of the soil data (for example, different spatial resolutions and soil depths), we harmonized all of the soil datasets by extrapolating the soil carbon stock to the full soil depth using two ensembles of empirical models for circumpolar and non-circumpolar regions, respectively, and by aggregating the datasets from the original spatial resolution to 0.5° (ref. [19]).

Four global vegetation biomass datasets were incorporated in this study. We combined the map of Thurner et al.[24] and Saatchi et al.[25] to produce a global map. The carbon stock of the tree stem was estimated based on the retrieved growing stock volume and using the BIOMASAR algorithm. The total carbon content of the vegetation was derived by summing roots, foliage and branches and tree stems. We used an updated version of vegetation from Saatchi et al.[25], which was derived using LiDAR, optical, microwave satellite images and trained on global in situ forest inventory plots. The above-ground biomass was obtained by extrapolating over the landscape using MODIS and radar imaging. The GlobBiomass[26] project provides above-ground biomass from a growing stock volume that is derived from space-borne backscattered intensity images and the BIOMASAR algorithm. We also used the global biomass map from Avitabile et al.[27] by fusing two maps using independent reference data from field observations[25,28].

We used FLUXCOM global carbon flux datasets, including GPP and TER, derived from three machine learning methods and two flux partitioning methods trained on daily carbon flux from over 200 flux tower sites using both satellite data and meteorological measurements[20]. GPP and TER were trained separately using three machine learning models with two different setups (remote sensing only and meteorological/climate forcing) as driver data to produce spatiotemporal grids of carbon flux. We averaged annual GPP and TER from 2001–2015 to derive mean annual maps.

We calculated the carbon turnover times in two different ways:

$$\tau = \frac{C_{\text{soil}} + C_{\text{veg}}}{\text{GPP}} \quad (3)$$

and

$$\tau = \frac{C_{\text{soil}} + C_{\text{veg}}}{\text{TER}} \quad (4)$$

Where both calculations are based on the assumption that the influx equals the outflux of carbon of the ecosystem (steady-state assumption). Since the GPP and TER products of FLUXCOM were trained independently, we used both equations (3) and (4) to estimate τ to better quantify the uncertainty that stems from different representations of carbon fluxes.

All of the datasets used in this study are harmonized to the same geographic coordinate system and spatial resolution of 0.5° using the mass conservative aggregation method, which guarantees that the carbon stocks of soil and vegetation do not change during aggregation from higher to low spatial resolution[19]. We produced the ensemble of 144 τ estimations in a full factorial manner by considering all of the possible combinations of three soil datasets at three different soil depths (1 m, 2 m and full soil depth), four vegetation datasets and four carbon flux datasets. This approach allows us to make a comprehensive assessment of the uncertainties in τ estimations that stem from different components of carbon pools in the whole ecosystem.

Site-level τ database

In this study, we used a site-level global τ database to estimate Q_{10} values and to quantify the potential H effect in parallel with the ensemble of τ estimates. At the site level, we estimated τ using in situ measurements of the total ecosystem carbon stock ($C_{\text{soil}} + C_{\text{veg}}$) and TER (equation (4)).

The Global Soil Respiration Database (SRDB)[29], downloaded on 10 December 2020 from https://github.com/bpbond/srdb, was used to obtain in situ soil respiration measurements. We also used Global Forest Ecosystem Structure and Function Data version 3.1 (GFESF)[30] to obtain TER in situ measurements (downloaded on 23 December 2020 from https://daac.ornl.gov/VEGETATION/guides/forest_carbon_flux.html). For both databases, we only used records that report annual TER and have geographic coordinates (longitude and latitude). The annual TER values are averaged if there are multiple measurements from different years for one site.

To obtain total soil carbon stock at the site level, we used the soil profile database provided by the World Soil Information Service (WoSIS)[31] and Northern Circumpolar Soil Carbon Database version 2 (NCSCDv2)[32]. The WoSIS soil profile database (downloaded on 18 December 2020 from https://doi.org/10.17027/isric-wdcsoils.20190901) contains over 190,000 soil profiles and provides soil organic carbon density, bulk density and fraction of coarse fragments data, which allow us to estimate the soil organic carbon stock (SOCS). We used an interpolation method to fill in the missing values of organic carbon density. The missing bulk density values are filled using median values of the measurements of all soil layers. The missing coarse fragments values are filled with zero (assuming no coarse fragment). The SOCS for each horizon can then be derived using

$$\text{SOCS} = \text{OC} \times \text{BD} \times \frac{100 - \text{CF}}{100} \times h \quad (5)$$

In the computation, the units of organic carbon density (OC), bulk density (BD) and coarse fragments (CF) are %, kg m^{-3} and %, respectively. The thickness of soil layer h is in metres. Therefore, the unit of SOCS is kg m^{-2}. The total soil carbon stock (C_{soil}) can then be derived by summing the SOCS of all soil layers. The NCSCDv2 database directly provides C_{soil} in both soil profile data and gridded data. We searched for matching geographic coordinates (latitude and longitude) in TER and C_{soil} databases to find sites with both measurements. We allowed a geographic proximity of 0.01° (~1 km) as the buffer to search for matching data points. Some sites in the SRDB report C_{soil} values retrieved

from literature. Note that we do not replace these records with WoSIS or NCSCDv2 but use the original values of C_{soil} for the analysis.

For sites that do not report C_{veg}, we fill the value with an estimation of C_{veg} based on satellite retrievals. Here, we use the global map of vegetation from Saatchi et al.[25], which has the highest spatial resolution (0.0083°) among all of the vegetation datasets we used in the study. Note that we do not replace the available in situ C_{veg} measurements that are reported in the SRDB and GFESF if both in situ- and remote sensing-derived data are available.

In addition to the two previous databases, we also incorporate a global network of eddy covariance sites (FLUXNET)[33] that provide annual TER, C_{soil} and C_{veg} measurements. The La Thuile FLUXNET dataset provides an additional 70 site-level measurements of τ. In total, we obtained 233 τ observations derived from different data sources.

At each site, the associated climate variables, including MAT and MAP, are retrieved from WorldClim2 high-resolution datasets at the same geographic coordinates[34]. The variable PET for each site is retrieved from the Global Aridity Index dataset[35,36]. The variable PSF for each site is retrieved from a global peatland map[37].

Exclusion of the data in deserts
We excluded grid cells of arid desert according to the Köppen–Geiger climate classification[38] BW (arid desert) since the carbon fluxes (GPP or TER) in deserts are negligible (close to zero) and therefore lead to unrealistic τ values. In total, we excluded ~5% of the global land area characterized by arid desert climate.

Climate, hydrometeorological and peatland cover datasets
The WorldClim2 (version 2) MAT, precipitation and long-term mean climate seasonality datasets were used in this study[34]. These climate variables were derived by assimilating worldwide ground weather station observations and remote-sensing covariates. The spatially interpolated gridded climate datasets have a spatial resolution of ~1 km and represent the mean climate condition from 1970–2000.

We used the Global Potential Evapotranspiration (Global–PET) dataset[35,36] to represent the ability of the atmosphere to remove water through evapotranspiration processes. The variables that are available from the WorldClim2 dataset, including minimum, maximum and average temperature, solar radiation, wind speed and water vapour pressure, were used in the Penman–Monteith equation to estimate PET. The dataset has a spatial resolution of ~1 km.

We used a global peatland map based on a meta-analysis of geo-spatial information from a variety of sources[37]. The global peatland distribution was derived by combining peatland-specific datasets at the global, regional and national level and the distribution of histosols derived from Harmonized World Soil Database v1.2, which resulted in a fine spatial coverage of PSF.

In this study, we used MAP, PET and PSF to represent different aspects of hydrological and hydrometeorological processes. The decomposition of ecosystem carbon (therefore τ) is largely affected by the soil moisture availability, which is determined by both water supply (MAP) and demand (PET). In fact, the ratio between MAP and PET is usually used to represent aridity[35]. In addition, the decomposition of soil carbon in peatland ecosystems is largely affected by the saturated moisture content due to low-level microbial activity, which can have a substantial influence on the temperature sensitivity[39].

Topography dataset. The ETOPO1 global topography dataset[40] was used in this study to investigate potential factors that may affect the spatial patterns of carbon turnover. An ETOPO1 relief model was generated from regional and global digital datasets that integrates land topography and ocean bathymetry.

Global land change dataset. We used the datasets of land cover change from Song et al.[41] to investigate its potential influence on carbon

turnover. The dataset includes variables such as percentages of tree canopy, short vegetation and bare ground, which were derived from Advanced Very-High-Resolution Radiometer remote-sensing measurements. The mean land cover change from 1982–2016 was used in this study as an explanatory variable in the analysis of linear regression (see Supplementary Information Section 2.2).

Derivation of Q_{10}
The traditional definition of Q_{10} used to describe the temperature sensitivity of instantaneous decomposition is as follows:

$$K(T) = K(T_{ref}) Q_{10}^{\left(\frac{T-T_{ref}}{\gamma}\right)} \tag{6}$$

Where $K(T_{ref})$ is the rate of decomposition at reference temperature T_{ref} and $K(T)$ is the rate of decomposition as a function of the environmental temperature. The parameters $\gamma = 10\,°C$ and $T_{ref} = 15\,°C$ are constants. Here, we adapted the conventional concept of Q_{10} for turnover processes by replacing K with turnover time:

$$K = \frac{1}{\tau} \tag{7}$$

Q_{10} with respect to turnover time then becomes:

$$\tau(T_{ref}) = \tau(T) Q_{10}^{\left(\frac{T-T_{ref}}{\gamma}\right)} \tag{8}$$

Here, τ is the ecosystem turnover time as a function of temperature and $\tau(T_{ref})$ is the reference turnover time at the reference temperature. We rewrite the equation by taking logarithms on both sides and deformation:

$$Q_{10} = 10^{-10\left(\frac{\log[\tau]-\log[\tau_{ref}]}{T-T_{ref}}\right)} \tag{9}$$

For each estimate of Q_{10} at a specific latitude or in a specific biome, a corresponding τ_{ref} is retrieved. Our key assumption is that τ_{ref} varies in space (that is, the reference turnover time variability is dependent on biomass, soil substrate availability, biome types and so on). Inferring Q_{10} in space then simplifies to a regression problem, although the form of regression may vary:

$$Q_{10} = 10^{-10\left(\frac{d\log[\tau]}{dT}\right)} \tag{10}$$

Previous studies have found both linear and polynomial (second-order) relationships between the two variables. We have shown that the nonlinearity in the $\log[\tau]$–temperature relationship is caused by H factors (see Supplementary Information Section 3). By controlling the H effect, we have shown a linear function of $\log[\tau]$ in response to temperature H factors supported by statistical analysis. Thus, the derivative of $\log[\tau]$ with respect to temperature can be represented by a linear function:

$$\log[\tau] = aT + b \tag{11}$$

Then, Q_{10} can be expressed as:

$$Q_{10} = 10^{-10a} \tag{12}$$

RDs of temperature and hydrology/hydrometeorology
To obtain RDs of each climate variable, we performed a similar but different regression from equation (2): all variables were standardized (z score), including logarithmic τ and all four climate variables so that each of the variables was centred to a mean value of zero and scaled

to have a standard deviation of 1. Following the previous study[42], we defined the RD of the effect of a climatic component x on the spatial variability of τ as the ratio between the mean variance of component x and the summed mean variance of all climatic components:

$$\text{RD}_x = \frac{\mu(\sigma^2(\tau_w^x))}{\mu\left(\sigma^2\left(\tau_w^{\text{MAT}} + \tau_w^{\text{MAP}} + \tau_w^{\text{PSF}} + \tau_w^{\text{AI}}\right)\right)}$$

Where τ_w^x is the product of a climatic component x (z score) and its corresponding coefficient (for example, $\tau_w^{\text{MAT}} = a_w^{\text{MAT}} \times$ z score (MAT)). The subscript w stands for different moving windows. In the case of global-scale analysis, w represents the whole global map (only one window). In the case of ecosystem-scale analysis, w represents different ecosystems. We calculated the RDs for each ensemble member at all spatial scales. The RD was calculated in the same manner across different spatial scales.

Moving window analysis

The responses of τ to different climate factors were assessed locally at each latitude by performing regression analysis using a 360° (in longitude) by 20° (in latitude) moving window. The 1st and 99th percentiles of data in each moving window were excluded to avoid the effect of outliers. To test the effect of window size on the results, we used a wide range of window sizes to confirm the robustness of our results (see details in Supplementary Information Sections 5 and 6).

Data availability

The ensemble τ database that supports the findings of this research is available from the data portal (https://doi.org/10.6084/m9.figshare.21187672.v3). The Köppen–Geiger climate classification map is available from http://koeppen-geiger.vu-wien.ac.at/present.htm. The WorldClim version 2 climate data are available from http://www.worldclim.com/version2. The Global Potential Evapotranspiration dataset is available from https://cgiarcsi.community/data/global-aridity-and-pet-database/#:~:text=The%20Global%20Potential%20Evapotranspiration%20(Global,PET%20Database%20is%20available%20here!. The peatland fraction data are available from https://peatdatahub.net/. Source data are provided with this paper.

Code availability

The code that was used to generate the results in this study is available upon reasonable request.

References

19. Fan, N. et al. Apparent ecosystem carbon turnover time: uncertainties and robust features. *Earth Syst. Sci. Data Discuss.* **12**, 2517–2536 (2020).
20. Jung, M. et al. Scaling carbon fluxes from eddy covariance sites to globe: synthesis and evaluation of the FLUXCOM approach. *Biogeosciences Discuss* **17**, 1343–1365 (2020).
21. Hengl, T. et al. SoilGrids250m: global gridded soil information based on machine learning. *PLoS ONE* **12**, e0169748 (2017).
22. Sanderman, J., Hengl, T. & Fiske, G. J. Soil carbon debt of 12,000 years of human land use. *Proc. Natl Acad. Sci. USA* **114**, 9575–9580 (2017).
23. Hengl, T. & Wheeler, I. Soil organic carbon stock in kg/m2 for 5 standard depth intervals (0–10, 10–30, 30–60, 60–100 and 100–200 cm) at 250 m resolution (v0.2). *Zenodo* https://zenodo.org/record/2536040#.Y1-jpVLP3t8 (2018).
24. Thurner, M. et al. Carbon stock and density of northern boreal and temperate forests. *Glob. Ecol. Biogeogr.* **23**, 297–310 (2014).
25. Saatchi, S. S. et al. Benchmark map of forest carbon stocks in tropical regions across three continents. *Proc. Natl Acad. Sci. USA* **108**, 9899–9904 (2011).
26. Santoro, M. & Cartus, O. Research pathways of forest above-ground biomass estimation based on SAR backscatter and interferometric SAR observations. *Remote Sens.* **10**, 608 (2018).
27. Avitabile, V. et al. An integrated pan-tropical biomass map using multiple reference datasets. *Glob. Change Biol.* **22**, 1406–1420 (2016).
28. Baccini, A. et al. Estimated carbon dioxide emissions from tropical deforestation improved by carbon-density maps. *Nat. Clim. Change* **2**, 182–185 (2012).
29. Bond-Lamberty, B., Bailey, V. L., Chen, M., Gough, C. M. & Vargas, R. Globally rising soil heterotrophic respiration over recent decades. *Nature* **560**, 80–83 (2018).
30. Luyssaert, S. et al. CO_2 balance of boreal, temperate, and tropical forests derived from a global database. *Glob. Change Biol.* **13**, 2509–2537 (2007).
31. Batjes, N. H., Ribeiro, E. & Van Oostrum, A. Standardised soil profile data to support global mapping and modelling (WoSIS snapshot 2019). *Earth Syst. Sci. Data* **12**, 299–320 (2020).
32. Hugelius, G. et al. A new data set for estimating organic carbon storage to 3m depth in soils of the northern circumpolar permafrost region. *Earth Syst. Sci. Data* **5**, 393–402 (2013).
33. Baldocchi, D. et al. FLUXNET: a new tool to study the temporal and spatial variability of ecosystem-scale carbon dioxide, water vapor, and energy flux densities. *Bull. Am. Meteorol. Soc.* **82**, 2415–2434 (2001).
34. Fick, S. E. & Hijmans, R, J. WorldClim 2: new 1-km spatial resolution climate surfaces for global land areas. *Int. J. Climatol.* **37**, 4302–4315 (2017).
35. Trabucco, A. & Zomer, R. J. Global aridity index and potential evapotranspiration (ET0) climate database v2. *Figshare* https://figshare.com/articles/dataset/Global_Aridity_Index_and_Potential_Evapotranspiration_ET0_Climate_Database_v2/7504448/3 (CGIAR CSI, 2019).
36. Zomer, R. J., Trabucco, A., Bossio, D. A. & Verchot, L. V. Climate change mitigation: a spatial analysis of global land suitability for clean development mechanism afforestation and reforestation. *Agric. Ecosyst. Environ.* **126**, 67–80 (2008).
37. Xu, J., Morris, P. J., Liu, J. & Holden, J. PEATMAP: refining estimates of global peatland distribution based on a meta-analysis. *Catena* **160**, 134–140 (2018).
38. Kottek, M., Grieser, J., Beck, C., Rudolf, B. & Rubel, F. World map of the Köppen–Geiger climate classification updated. *Meteorol. Z.* **15**, 259–263 (2006).
39. Paavilainen, E. & Päivänen, J. *Peatland Forestry: Ecology and Principles* (Ecological Studies Book 111, Springer Science & Business Media, 1995).
40. Amante, C. & Eakins, B. W. *ETOPO1 Arc-Minute Global Relief Model: Procedures, Data Sources and Analysis* (NOAA, 2009).
41. Song, X.-P. et al. Global land change from 1982 to 2016. *Nature* **560**, 639–643 (2018).
42. Jung, M. et al. Compensatory water effects link yearly global land CO_2 sink changes to temperature. *Nature* **541**, 516–520 (2017).

Author contributions

N.F. and N.C. designed the analysis of this research in collaboration with B.A. and M.R. N.F. conducted the analysis and wrote the manuscript with contributions from all authors.

Funding

Competing interests

Additional information

Ecosystem turnover times

Uncertainty

Extended Data Fig. 1 | Spatial patterns of τ and the uncertainty. Spatial distribution of ensemble median τ (upper) and its relative uncertainty (interquartile range/mean) across different ensemble members (bottom).
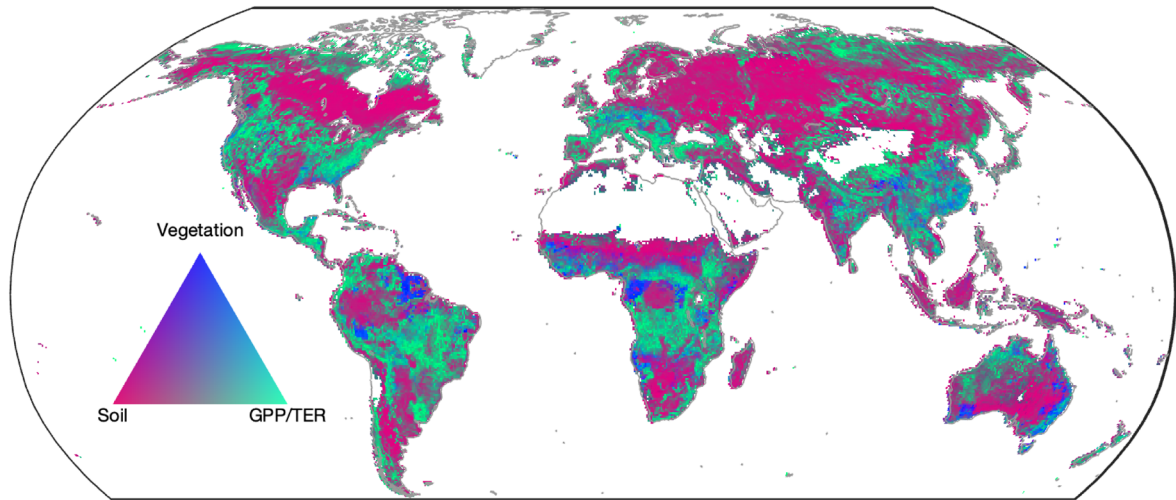
Extended Data Fig. 2 | Contribution to the τ uncertainty from different ecosystem components. Different color indicates the grid cells where the uncertainty is dominated by soil carbon (64.3 % of total land area), GPP/TER (34.4% of total land area) and vegetation carbon (1.3% of total land area), respectively.
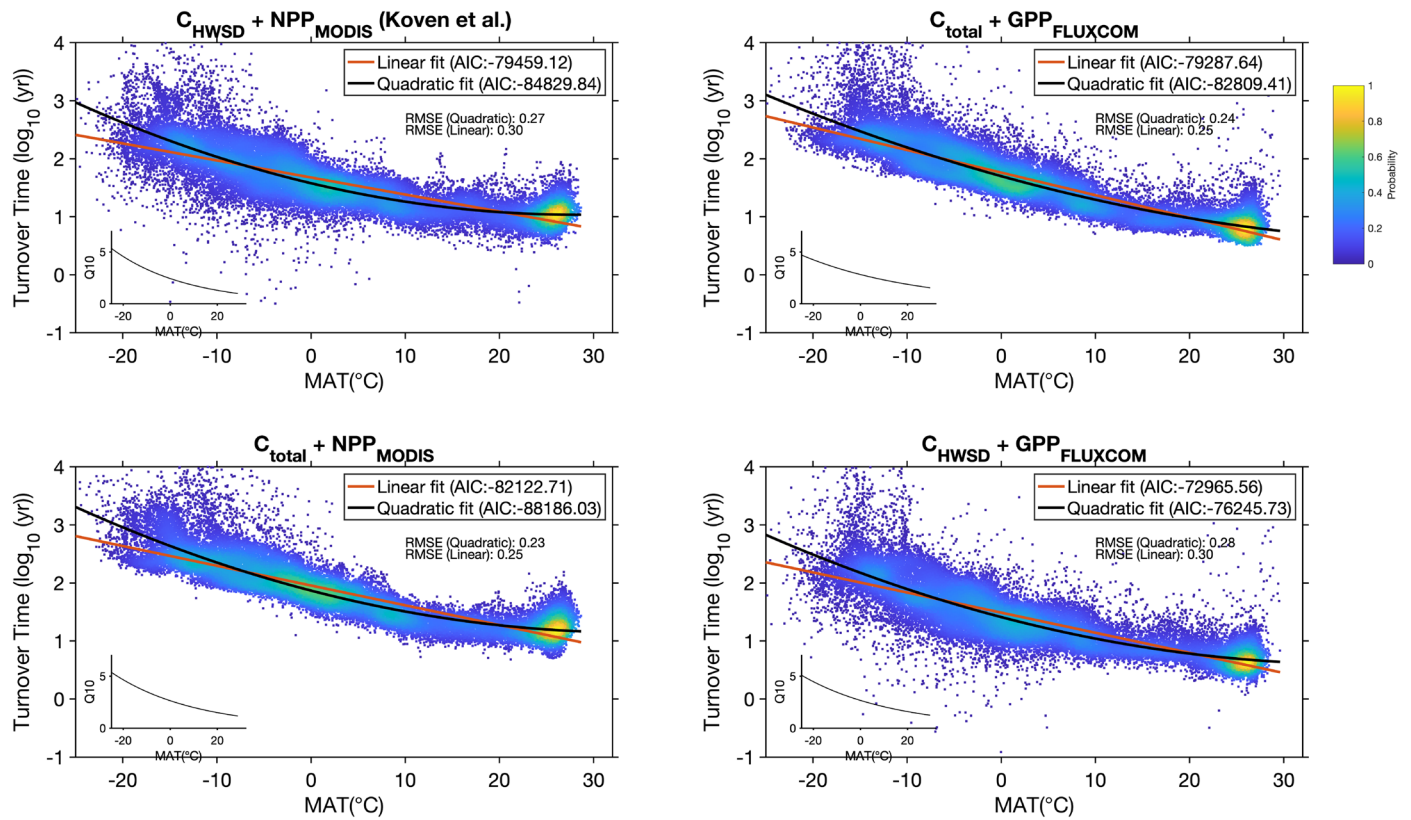
Extended Data Fig. 3 | Comparison between fittings of log (τ) as a function of temperature with linear and quadratic models and corresponding Q_{10} values on global scale. Solid black lines represent quadratic fitting curves (log10(τ) ~ MAT²+MAT) while red lines represent linear fit (log10(τ) ~ MAT). The density plot of observational data is overlaid. The embedded smaller figure at the lower left corner is Q_{10} values (derived from quadratic fitting) against temperature. Different data is used to estimate τ with two different carbon stocks (C_{total} and C_{HWSD}) and two carbon flux products (GPP_{MODIS} and $GPP_{FLUXCOM}$).
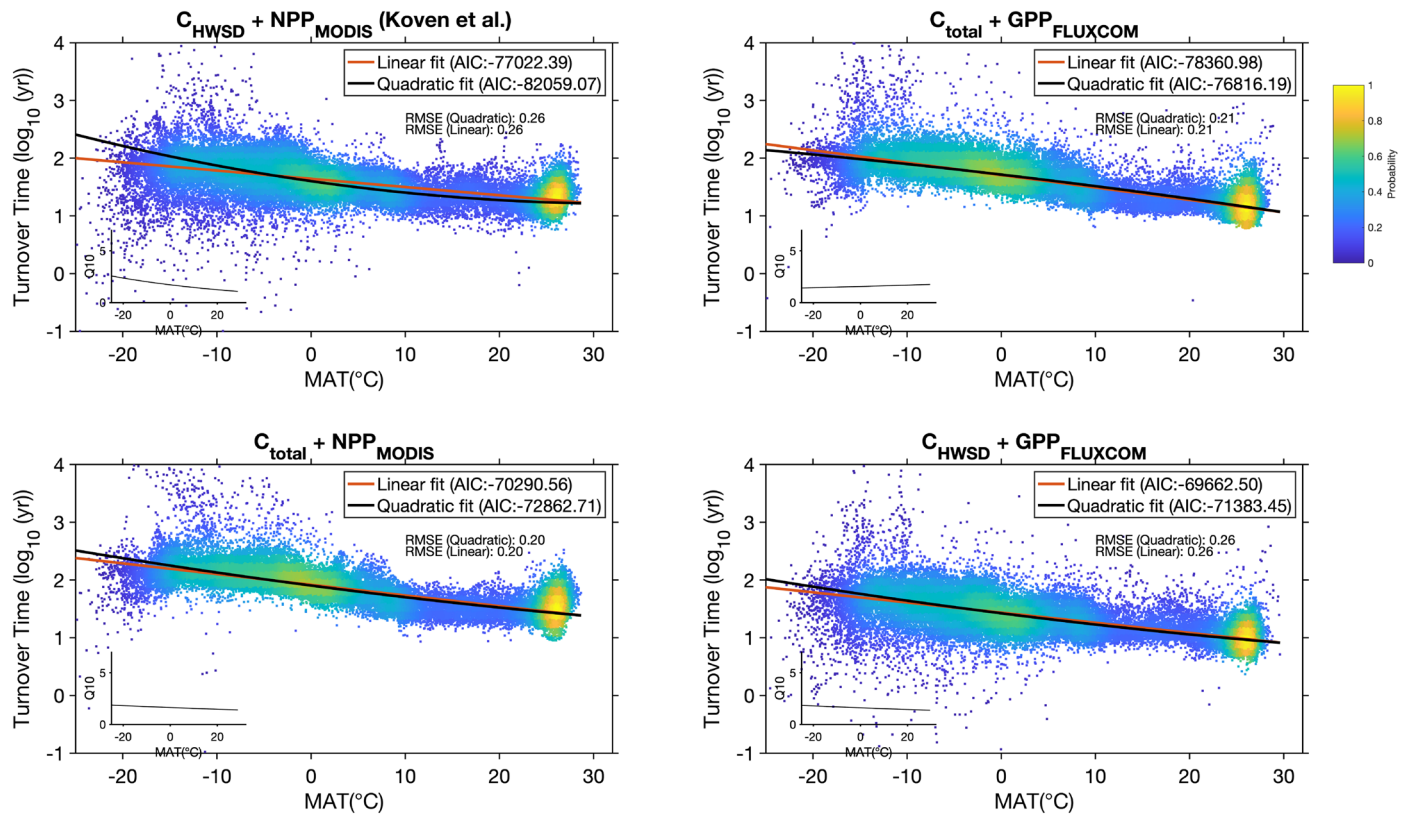
Extended Data Fig. 4 | The adjusted response of log (τ) to MAT when the hydrometeorological effect is controlled in multiple regression models. Solid black lines represent quadratic fitting curve (log10(τ) ~ MAT²+MAT+1/MAP+1/PET+PSF) while red lines represent linear fit (log10(τ) ~ MAT+1/MAP+1/PET+PSF). The density plot (overlaid) shows the adjusted response of log(τ) to MAT when the average conditions of the other predictors are taken into account. The embedded smaller figure at the lower left corner is Q_{10} values (derived from quadratic fitting) against temperature. Different data is used to estimate τ with two different carbon stocks (C_{total} and C_{HWSD}) and two carbon flux products (GPP_{MODIS} and $GPP_{FLUXCOM}$).

Extended Data Table 1 | Comparison of model performances between equation (1) (using only *T* as a predictor) and equation (2) (using both *T* and H factors as predictors) using both global ensemble and site-level datasets

.

	Ensemble median		
	R2	RMSE	AIC
Eq.1	0.77	0.24	-119131.87
Eq.2	0.84	0.21	-119914.36
	Site-level		
	R2	RMSE	AIC
Eq.1	0.30	0.37	-467.19
Eq.2	0.35	0.36	-473.21